

High Rate Hybrid MnO₂@CNT Fabric Anode for Li-Ion Batteries:

Properties and Lithium Storage Mechanism by In-Situ Synchrotron X-Ray Scattering

Moumita Rana,^a Venkata Sai Avvaru,^b Nicola Boaretto,^{a,c} Víctor A. de la Peña O'Shea,^d

Rebeca Marcilla,^c Vinodkumar Etacheri^{*a} and Juan J. Vilatela^{*a}

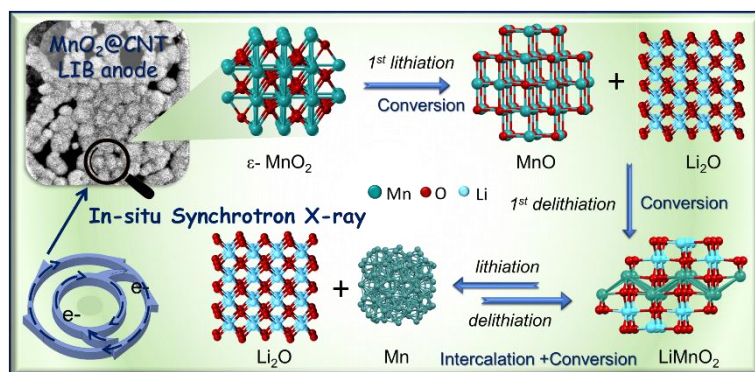
^aIMDEA Materials, Eric Kandel 2, 28906 Getafe, Madrid, Spain

^bFaculty of Science, Autonoma University of Madrid, C/ Francisco Tomás y Valiente, 7, Madrid 28049, Spain

^cIMDEA Energy, Avda. Ramón de la Sagra 3, 28935 Móstoles, Madrid, Spain

^dPhotoactivated Processes Unit, IMDEA Energy Institute, Avda. Ramón de la Sagra 3, Parque Tecnológico de Móstoles, 28935 Móstoles, Madrid, Spain.

* vinodkumar.etacheri@imdea.org, juanjose.vilatela@imdea.org



Abstract: High-performance anodes for rechargeable Li-ion battery are produced by nanostructuring of the transition metal oxides on a conductive support. Here, we demonstrate a hybrid material of MnO₂ directly grown onto fabrics of carbon nanotube fibres, which exhibits notable specific capacity over 1100 and 500 mAh/g at a discharge current density of 25 mA/g and 5 A/g, respectively, with coulombic efficiency of 97.5 %. Combined with 97 % capacity retention after 1500 cycles at a current density of

5 A/g, both capacity and stability are significantly above literature data. Detailed investigations involving electrochemical and in situ synchrotron X-ray scattering study reveal that during galvanostatic cycling, MnO_2 undergoes an irreversible phase transition to LiMnO_2 , which stores lithium through an intercalation process, followed by conversion mechanism and pseudocapacitive processes. This mechanism is further confirmed by Raman spectroscopy and X-ray photoelectron spectroscopy. The fraction of pseudocapacitive charge storage ranges from 27% to 83%, for current densities from 25 mA/g to 5 A/g. Firm attachment of the active material to the built-in current collector makes the electrodes flexible and mechanically robust, and ensures that the low charge transfer resistance and the high electrode surface area remain after irreversible phase transition of the active material and extensive cycling.

1. Introduction:

Lithium ion battery (LIB) is a crucial technology for most envisaged renewable energy schemes. Owing to their high energy density, wide voltage range they can be integrated in applications ranging from portable electronics to large-scale grids.^{1,2} In the context of the electric mobility, LIBs have widespread use in automobiles and are the benchmark of current efforts for electric aircraft.^{3,4} In electric transport, in addition to the ever-increasing need for higher specific energy density, there is particularly strong interest in performance at high rates in order to enable fast charge/discharge,⁵⁻⁷ and in new battery concepts with augmented mechanical properties that provide: improved fatigue resistance and flexibility⁸⁻¹⁰, enabled integration into existing structural components, use as load-bearing elements (i.e. structural batteries).^{7,11,12}

Transition metal oxides (TMO) have shown promising activity as conversion materials for LIB.¹³ Among them, manganese oxides stand out due to their high theoretical capacity (e.g. MnO, Mn₃O₄, Mn₂O₃, and MnO₂ have theoretical capacity of 756, 937, 1018, and 1230 mAh g⁻¹ respectively)¹⁴ and a lower operating potential compared to Fe-, Co-, and Ni based transition metal oxides.^{15,16} Nano-structuring of TMOs increases their high surface area, which in turn results in significantly high specific capacity from pseudocapacitive processes. This “hybrid” energy storage mode produces high capacity at high current densities.^{17,18} Maier and coworkers, for example, have demonstrated a 60% enhancement in specific capacity in nanoporous anatase TiO₂ compared to the same bulk material, when used as LIB anode.¹⁹

However, there are several challenges associated with TMO electrodes for LIB that prevent us from exploiting their full potential. From the point of view of fabrication, it is straightforward to deposit nanostructured TMOs on a conventional metallic current collector (e.g. Al, Cu), but the resulting interface is very poor and cannot withstand the large structural (volume) change in TMO during charge/discharge cycles, leading to agglomeration and sintering of nanostructures.²⁰⁻²³ This agglomeration can significantly reduce capacity due to a lower surface for pseudocapacitive processes and slower lithium diffusion kinetics. A more promising strategy is to stabilise the TMO onto a porous network of nanocarbons, either carbon nanotubes (CNT) or graphene.^{1,24-29} The synthetic strategies for Lithium ion battery (LIB) is a crucial technology for most envisaged renewable energy schemes. Owing to their high energy density, wide voltage range they can be integrated in applications ranging from portable electronics to large-scale grids.^{1,30,31} In the context of the electric mobility, LIBs have widespread use in automobiles and are the benchmark of current efforts for electric aircraft.^{3,4} In electric transport, in addition to the ever-increasing need for higher specific energy density, there is particularly strong interest in performance at high rates in order to enable fast charge/discharge.³²⁻³⁴ Moreover in new battery concepts with augmented mechanical properties are gathering huge attention since they

provide: improved fatigue resistance and flexibility,^{8–10,35} enabled integration into existing structural components, and use as load-bearing elements (i.e. structural batteries).^{11,12}

Transition metal oxides (TMO) have shown promising activity as conversion materials for LIB.¹³ Among them, manganese oxides stand out due to their high theoretical capacity (e.g. MnO, Mn₃O₄, Mn₂O₃, and MnO₂ have theoretical capacity of 756, 937, 1018, and 1230 mAh g⁻¹ respectively)¹⁴ and a lower operating potential compared to Fe-, Co-, and Ni based transition metal oxides.^{15,16} Nano-structuring of TMOs increases their specific surface area, which in turn results in significantly high specific capacity from pseudocapacitive processes.³⁶ This “hybrid” energy storage mode produces high capacity at high current densities.^{18,37} Such strategy also leads to substantial improvement in power performance and cycling behaviour due to shorter ion diffusion paths and facilitating Li insertion with minimized internal strain.^{14,38} Maier and coworkers, for example, have demonstrated a 60% enhancement in specific capacity in nanoporous anatase TiO₂ compared to the same bulk material, when used as LIB anode.¹⁹ For manganese dioxide, α -MnO₂ nanorods demonstrated significantly enhanced electrochemical performance with initial reversible capacity of 1075 mAh g⁻¹ at current density of 0.1 A g⁻¹,³⁹ and a 3D δ -MnO₂ mesopore nanostructure delivered a high lithium storage capacity of 905 mAh g⁻¹ at 0.1 A g⁻¹ with a capacity retention of 94% after 200 cycles at 1 A g⁻¹.¹⁸

However, there are several challenges associated with TMO electrodes for LIB that prevent us from exploiting their full potential. From the point of view of fabrication, it is straightforward to deposit nanostructured TMOs on a conventional metallic current collector (e.g. Al, Cu), but the resulting interface is very poor and cannot withstand the large structural (volume) change in TMO during charge/discharge cycles, leading to agglomeration and sintering of nanostructures.^{20–23} This agglomeration can significantly reduce capacity due to a lower specific surface area for pseudocapacitive processes and slower lithium diffusion kinetics. A more promising strategy is to stabilise the TMO onto a porous network of nanocarbons, either carbon nanotubes (CNT) or graphene.^{1,24–29} The synthetic strategies for the preparation of CNT fiber based hybrids mostly rely on the in situ growth of nanocrystals on the CNTF by electrodeposition, sol-gel, electroless deposition, solvothermal and high temperature vapour deposition methods.^{26,40} Such strategies not only result in an electrochemically stable interface between metal oxide and carbon support, but also helps to avoid the use of polymeric binders during electrode preparation. As an example, nanostructured MnO₂ directly grown onto unidirectional fabrics of CNT fibres resulted in pseudocapacitive electrodes with high capacitance, stability above 6000 cycles under high potential, and large mechanical robustness, stemming from the strong adhesion of the TMO to the built-in CNT fabric current collector.⁴¹

More importantly, stabilising nanostructured TMOs onto porous CNT current collectors can enable a detailed study on their structural changes when used as LIB electrodes, a necessary step towards further improvements in performance and cyclability. The vast number of works on

performance of MnO₂ LIB anodes contrasts with very few studies on the mechanism of lithium storage in MnO₂ anodes. Specifically, when TMOs are employed as anodes, the conversion process during charge-discharge is often assumed to be a reversible transformation of the parent TMO to Li₂O and metal.^{42,43} On the other hand, experimental studies reveal a far more complex process because of the various possible phase transformations and microstructural changes of the TMO. Using electron energy loss spectroscopy and selected area electron diffraction analysis, Chen *et al.* proposed that β -MnO₂ is only partially reduced to LiMn₃O₄, instead of being reduced to metallic Mn.⁴⁴ From ex-situ X-ray diffraction study, Fang *et al.* found that lithiation of MnO₂ results in Li_xMnO₂ (x=0.96) and Li₂MnO₂, which is further reduced to metallic Mn and Li₂O at 0 V,⁴⁵ consistent with observations by other groups.⁴⁶ However, after complete delithiation at 3.0 V, MnO was found to be the end product.⁴⁵ Such permeant reduction of Mn⁴⁺ to lower oxidation state (+2) during the charge-discharge cycle reduces specific capacity after cycling. Contrary to this experimental evidence of permanent phase transformation during charge/discharge, it is common to find the widespread assumption of a reversible conversion of MnO₂ based solely on voltammetric profiles.^{39,47}

Herein, we perform in situ synchrotron X-ray scattering measurements during lithium storage in the hexagonal phase (Akhtenskite) of MnO₂. We synthesized free-standing ϵ -MnO₂-CNT fibre hybrids (MnO₂@CNTF) by producing a uniform coating of porous MnO₂ flower-like nanostructures around bundles of CNT. When used as an anode in half-cell configuration against Li-metal, this material shows specific capacity of 1153, 519 and 344 mAh/g at scan rates of 25 mA/g, 5 and 10 A/g respectively, a rate capability above that of most related materials. At low scan rate, the lithium storage process occurs through a conversion mechanism, whereas at high scan rate the mechanism mostly relies on pseudocapacitive Li storage. In situ synchrotron X-ray scattering study reveals that during the first charge-discharge cycle, the hexagonal structure of parent MnO₂ slowly converts to lithiated manganese oxide. In the consecutive galvanostatic cycles, this structure undergoes a reversible phase transformation with Li₂O and Mn. During this process the porous MnO₂ structures experience ‘electrochemical milling’, forming a nanoscopic thin oxide coating around the CNT bundles that leads up to 200% increase in the specific capacity of the material.

Experimental Details

Chemicals

Butanol, Ferrocene. Sodium nitrate (99.99%, Sigma Aldrich), Manganese nitrate (99.9%, Merck), Li metal sheet, 1 M LiPF₆ in ethylene carbonate and ethyl methyl carbonate (1:1-v/v, Sigma Aldrich), Manganese oxide ($\geq 99\%$, Sigma Aldrich). All chemicals were used as received, without further purification.

Synthesis of free standing CNT fiber veils

The CNT fiber (CNTF) veils were prepared by chemical vapour deposition method at 1250 °C under hydrogen atmosphere in a vertical tube furnace using butanol, ferrocene and thiophene as carbon source, catalyst and promoter respectively.⁴⁸ The CNTF veil electrodes were prepared by winding the CNT fibers around a paper spool for 30 minutes, which was later taken out from the spool as free standing electrode. The aerial density of the samples was estimated to be ~ 0.7 mg/cm². The CNT fibres used in this work have a specific surface area ~250 m²/g and longitudinal conductivity around 3.5×10⁵ S/m.⁴⁹

Electrodeposition of MnO₂ on CNTF

The free-standing CNT fiber veils were electrochemically oxidized by using chronoamperometry at a constant voltage of 2.5 V for 1 minute in 0.1 M Na₂SO₄.⁵⁰ The functionalized CNTF veils were rinsed with water and subjected to electrodeposition using a solution of NaNO₃ (255mg) and Mn(NO₃)₂ (600 mg) in water-ethanol (30 mL, 1:1) mixture as electrolyte. The electrodes were produced under chronopotentiometric conditions with a constant current density of 300 μA/cm² for 1 hour, followed by thorough washing with water and ethanol. The electrodeposited samples were annealed in air at 120 °C for over-night. The mass fraction of MnO₂ can be adjusted by varying electrodeposition parameters. The conditions used here were selected to yield a mass fraction in the range 40-65%. To estimate the weight saving factor, we prepared a reference material by coating a dispersion of commercial MnO₂, acetylene black, PVDF (7:2:1) on a Cu foil. The electrode was dried in oven at 80 °C under vacuum for overnight and used for electrochemical measurements.

Characterizations

The samples were characterized using field effect scanning electron microscopy (FESEM, FEI Helios NanoLab 600i), transmission electron microscopy (TEM, Talos F200X FEG, 200 kV), selected area electron diffraction (SAED), high-angle annular dark-field imaging- energy-dispersive X-ray spectroscopy (HAADF-EDS), Raman spectroscopy (Ranishaw, fitted with a 532 nm laser source), thermogravimetric analysis (TGA, Q50, TA Instruments), Brunauer-Emmett-Teller (BET) adsorption (Micromeritics, TriStar II Plus Version 3.01), wide angle X-ray scattering (WAXS, CDD detector LX255-HS, Rayonix) and Near Ambient Pressure X-ray photoelectron spectroscopy (NAP-XPS SPECS System, Al Kα monochromated source and 1-DLD detector).

Electrochemical Measurements

The samples were tested as working electrode in coin cell configuration (type 2032). Li metal plates were used as reference and counter electrode, glass fiber (Whatmann) as separator, and 1 M LiPF₆ solution in a mixture of EC-EMC (1: 1 v/v) was used as electrolyte. The coin cells

were assembled in glove box, filled with argon (concentration of O₂ and H₂O < 1.0 ppm). The charge storage behaviour of the sample was characterized by charge-discharge (CD) using Neware battery testing unit, cyclic voltammetry (CV) and electrochemical impedance spectroscopy (EIS) using Biologic SP-200 electrochemical workstation. The voltages mentioned throughout the manuscript is with respect to Li/Li⁺ redox potential.

In situ measurements

In situ synchrotron WAXS measurements were performed using a home-made gas-tight teflon cell, fitted with two kapton windows. The sample was placed at the centre of the windows and connected to the external cables through metallic tape. The electrochemical measurements were performed in a two electrode configuration. The experiments were performed at the Non Crystalline Diffraction (NCD-SWEET) beamline 11 of ALBA Synchrotron Light Facilities. The WAXS patterns were calibrated using chromium (III) oxide (Cr₂O₃) EAXS pattern as reference. Radial profiles were obtained after azimuthal integration of scattering intensity.

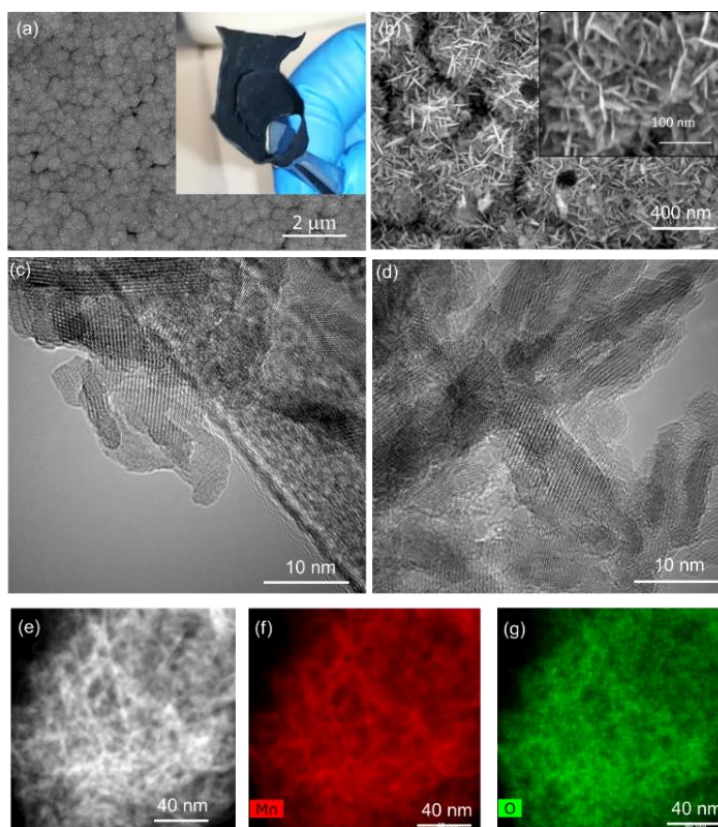


Figure 1. (a, b) FESEM images of MnO₂@CNT showing uniform growth of nanostructured hollow MnO₂ flowers on CNT fiber veils. Inset in (a) shows the flexible nature of macroscopic MnO₂@CNT hybrid. Inset in (b) shows high-resolution image of interconnected nanopetals. (c, d) TEM images of the hybrid showing the growth of polycrystalline nanopetals of MnO₂ on functionalized CNT. (e) HAADF and (f, g) EDS elemental mapping images corresponding to elements Mn and O respectively of a MnO₂ flower.

Results and Discussion:

Free-standing hybrid MnO_2 @CNT fabrics were prepared by electrodepositing manganese oxide on electrochemically pre-functionalized CNT fiber fabrics from a solution of manganese nitrate in water and ethanol mixture (1:1).^{41,50} The FESEM images of the sample at different magnifications are shown in **Figure 1a-d**. The inset in **Figure 1a** shows the flexible nature of the macroscopic electrode sample, which can withstand rolling up to a radius < 8 mm. The CNTF is uniformly covered by the porous flower-like nanostructures with average diameter of 550 nm (± 100), comprised of interconnected thin sheets with thickness of ~ 13 nm (± 6) and length of 50-100 nm (**Figure 1a, b** and **Figure S1**), resembling petals.

These nanocrystals are predominantly aligned with their main axis perpendicular to the CNT bundles and aggregated into semi-spherical structures, as shown in **Figure 1b** and **S1e**. The uniform growth of the manganese oxide nanostructures on CNTF can be related to the mild pre-oxidation of the CNT fibers by electrochemical functionalization, as the same electrodeposition treatment on the pristine CNT samples leads to only partial coverage of the fibers by larger manganese oxide porous structures, as shown in **Figure S2**. The oxygen functional groups at the CNT surface apparently act as nucleation sites for the deposition of metal oxide during chronopotentiometric process, thereby facilitating uniform growth of the smaller size flowers. As key features of this type of electrodes we highlight the large size, strength and low electrical resistance of the interface between MnO_2 and the CNT bundles. For the samples in this study, no evidence of detachment of MnO_2 has been observed after extensive manipulation and repeated bending, in agreement with recent reports on related hybrids used for LIB cathodes and

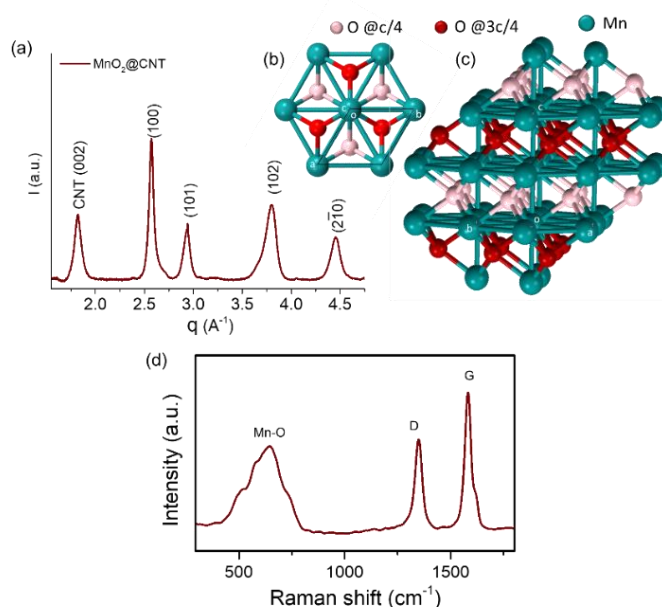


Figure 2. (a) Synchrotron X-ray diffraction pattern of the MnO_2 @CNTF hybrid. (b, c) Crystal structure of the hexagonal Akhtenskite phase of MnO_2 along (b) and perpendicular (c) to the c -axis. (d) Raman spectra of MnO_2 @CNTF hybrid.

which combine exceptional mechanical toughness and a 29 % increase in specific capacity compared to commercial LIB cathodes, preserved even after tensile fracture.⁵¹

Figure 1c and d show the high resolution TEM images of the MnO₂@CNTF hybrid. Under TEM, the “petals” of the manganese oxide appear as polycrystalline layer of manganese oxide. In **Figure 1c**, the high-resolution image of the CNT- manganese oxide interface reveals that, these nanocrystals are directly attached to the CNT surface. To investigate the elemental composition of this hybrid, we performed HAADF-EDS mapping. **Figure 1e-g** shows the HAADF image and elemental mapping of the same particle corresponding to manganese and oxygen. BET isotherm analysis was performed to estimate surface area of the MnO₂@CNTF hybrid. **Figure S3b** shows isothermal adsorption and desorption profiles of N₂ at 77K, which can be assigned as type II. The surface area of the MnO₂@CNTF was found to be 130 m²/g.

In order to understand the crystal structure, we have acquired the synchrotron XRD pattern of the MnO₂@CNTF hybrid, as shown in **Figure 2a**, which can be indexed on the basis of the hexagonal Akhtenskite phase of MnO₂ with lattice parameters $a = b = 2.829 \text{ \AA}$, $c = 4.410 \text{ \AA}$ ($c/a = 1.559$) and $\alpha = \beta = 90^\circ$ and $\gamma = 120^\circ$ with a space group of P6₃/mmc.^{52,53} In **Figure 2b and c** the crystal structure of this phase is shown along and perpendicular to c-axis respectively. In this structure, the Mn⁴⁺ ions occupy the corners as well as centre of the edges at $\frac{1}{2} c$ distance, and the hexa-coordinated O²⁻ ions occupy alternate octahedral sites.

Figure 2d shows the Raman spectra of MnO₂@CNTF hybrid. The two sharp peaks at 1352.8, 1582.3 cm⁻¹ can be assigned to D and G bands of oxygen functionalized CNT fibers respectively, which are originated from disordered features of CNT and tangential vibrational mode displacement (E2g mode) respectively. Here the I_D/I_G ratio of the functionalized CNT was found to be 0.75. The peaks at 645, 583 and 530 cm⁻¹ can be attributed to the symmetric stretching and bending modes of Mn-O in [MnO₆] octahedra.⁵⁴ The high intensity of such MnO₂ peaks confirms the extensive coverage of the CNTF by crystalline MnO₂.^{55,56} To estimate the loading of MnO₂ in the hybrid, we performed thermogravimetric analysis in aerial atmosphere and calculated mass fraction taking into account the catalytic combustion of CNT in presence of chemically attached Mn-O bonds.⁵⁷ (**Figure S4**). The sample analysed in this work has a mass fraction of MnO₂ of 55 wt.%, which we found to provide a good balance between electrochemical properties and mechanical robustness.

Electrochemical performance

The lithium storage capacity of MnO₂@CNTF hybrid was estimated using a coin cell configuration with Li foil as counter electrode. The open circuit voltage (OCV) of the pristine cell was measured to be 3 V (vs. Li/Li⁺). **Figure 3a** shows the first two cyclic voltammograms at a scan rate of 0.1 mV/s. The initial cathodic profile (lithiation) contains a strong peak at 0.12 V corresponding to conversion of Mn⁴⁺ to metallic Mn.⁵⁸ An additional cathodic peak at 0.65 V

with a small hump at 0.78 V can be attributed to the formation of solid electrolyte interphase (SEI).⁵⁹ In the following anodic cycle (delithiation), two peaks were observed at 1.27 and 2.19 V, which can be attributed to the oxidation of Mn^0 to Mn^{2+} and Mn^{2+} to higher oxidation states of Mn ($\text{Mn}^{3+}/\text{Mn}^{4+}$) respectively.⁵⁸ Interestingly, in the 2nd cathodic profile the cathodic peaks appeared at 0.31 and 0.20 V, which are distinctly different from the first cycle. Such higher lithiation voltage of MnO_2 after the first cycle is indicative of an irreversible structural change of the oxide layer, taking place during the first redox cycle.^{45,60} In the 2nd delithiation process the anodic peaks were observed almost at the same position as that of the first one (1.31 and 2.21 V). For reference, we performed cyclic voltammetry using pristine CNT as anode under identical conditions, which was found to be distinctively different from that of $\text{MnO}_2@\text{CNTF}$ hybrid (**Figure S5a**).

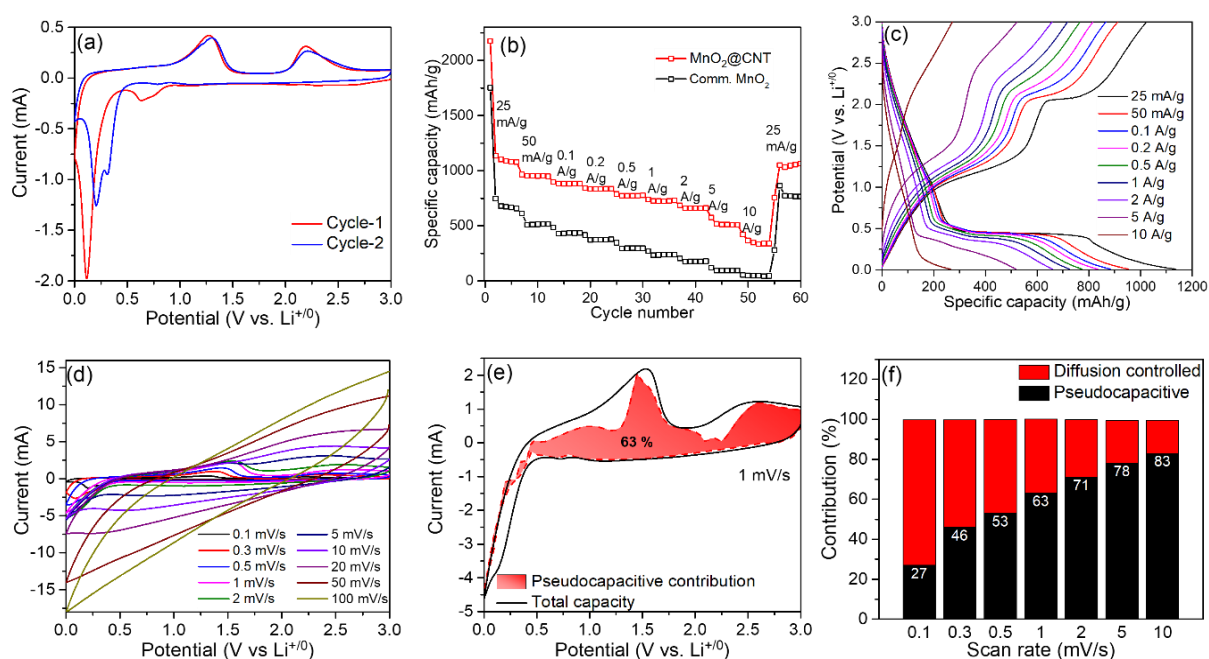


Figure 3. (a) First two cyclic voltammograms of $\text{MnO}_2@\text{CNTF}$ hybrid at a scan rate of 0.1 mV/s. (b) Rate profiles of $\text{MnO}_2@\text{CNTF}$ hybrid and commercial MnO_2 at current densities of 25 mA/g to 10 A/g. (c) Voltage profiles of $\text{MnO}_2@\text{CNTF}$ hybrid corresponding to its rate profile in (b). (d) cyclic voltammograms of $\text{MnO}_2@\text{CNTF}$ hybrid at different scan rates. (e) Deconvoluted contribution of pseudocapacitive processes in the cyclic voltammograms at a scan rate of 1 mV/s. (f) Estimated contribution of diffusion controlled and pseudocapacitive reactions with different scan rates.

The redox features of $\text{MnO}_2@\text{CNTF}$ hybrid from cyclic voltammograms are in complete accordance with the galvanostatic charge-discharge (CD) profiles. The discharge capacity

values of MnO₂@CNTF at current densities 25 mA/g to 10 A/g are shown in **Figure 3b**. **Figure S5b** shows the first three CD profiles of the MnO₂@CNTF at current density of 25 mA/g. In the first discharge process (lithiation), the specific capacity of MnO₂@CNTF hybrid was found to be 2175 mAh/g, dropping to 1153 mAh/g after the second cycle and remain fairly stable afterwards. Such decrease in the specific capacity in the first cycle can be attributed to the irreversible consumption of lithium in the formation of SEI layer as well as partial lithiation of manganese oxide (*vide infra*). The specific capacities of MnO₂@CNTF at current densities of 0.1, 1, 5 and 10 A/g were found to be 882, 722, 519 and 344 mAh/g respectively. Even though the transition metal oxides are well known for their high Li-ion storage capacity at low current density, such a high capacity at high current density is quite impressive for these materials. For reference, we compared the rate profile of commercial MnO₂ in Figure 3b (and Figure S6). The specific capacity values were estimated to be 680, 434, 236 and 93 mAh/g at current densities of 0.025, 0.1, 1 and 5 A/g respectively, which are much lower with respect to the performance of our MnO₂@CNTF hybrid. When compared with the literature reports on high performance Li-ion storage material, this MnO₂@CNTF hybrid exhibits performance well above average for all current densities, and to our knowledge, the highest value reported at high current density for MnO₂ as starting anode material. (see the comparison **Table ST1** and **Figure S5d** in ESI).

The voltage profiles of the material at various current densities are shown in **Figure 3c**. For each particular current density, the voltage profiles were found to be near identical, with coulombic efficiency > 97.5%. This confirms that after the irreversible transformation in the first cycle, subsequent charge-discharge cycles are fairly reversible. We also note that the redox features of these CD profiles are significantly different from the same of pristine CNT fiber electrode (**Figure S5a**), confirming the predominant contribution of MnO₂ in the charge storage mechanism.

The voltage profiles of the lithiation process at lower current densities have three distinct regions: (i) an almost linear voltage decrease from 3V to 0.45 V, (ii) a flat plateau around 0.45 V, followed by (iii) a sloping profile up to complete lithiation. The plateau in region (ii) is representative of the conversion reaction of manganese oxide, whereas the presence of the sloping profiles in regions (i) and (iii) are a signature of pseudocapacitive Li storage at the inorganic material surface and at newly formed Li₂O –metal interface, respectively.⁶¹ With increasing current density, the plateau-like feature (region ii) decreases and finally merges with the region (iii). In order to estimate the contribution of conversion reaction and pseudocapacitive processes towards total Li-ion storage capacity at different current densities, we performed CVs at different scan rates (**Figure 3d**). When the scan rate is higher than 5 mV/s, the redox peaks are hardly distinguishable, thus indicating negligible contribution from diffusion controlled conversion reactions. We calculated the contribution of capacity from diffusion controlled conversion reactions and pseudocapacitive surface reactions using the following equation.^{36,62,63}

$$I(V) = K_1v + K_2v^{1/2} \quad (\text{eq. 1})$$

Where v is the scan rate, and K_1 and K_2 are scan rate independent constants. K_1v stands for capacitive contribution and $K_2v^{1/2}$ denotes diffusive contribution. As shown in **Figure 3e**, at a scan rate of 0.1 mV/s (nearly equivalent to a current density of 100 mA/g), the contribution of the diffusion-controlled reaction (i.e. conversion reaction) is as high as 73%, which decreases to 17% at a high scan rate of 10 mV/s (comparable to lithiation in galvanostatic control at current density of 5 A g⁻¹, **Figure 3f**). This shows that at low current density, the charge storage mechanism mostly occurs through conversion process, whereas at high current densities, it is based on pseudocapacitive surface reactions only.

The high rate performance of MnO₂@CNTF can be mostly ascribed to high surface area of the oxide layer around the CNTF, which itself has a high specific surface area (SSA) of 250 m²/g.⁴⁹ In addition to templating the growth of the metal oxide, the highly conducting porous CNT fibre support can buffer the structural change of MnO₂ active material during the conversion reactions, which would otherwise undergo irreversible agglomeration, thereby significantly compromising on the charge storage capacity in the following cycles and producing unstable rate profiles.⁶⁴

Lithium storage mechanism in ϵ -MnO₂:

To understand the structural changes of manganese dioxide layer during the lithiation/delithiation process, we performed in situ synchrotron WAXS measurements using a gas-tight teflon cell, fitted with two kapton windows, built in-house (**Figure S7**). The OCV of the pristine device was recorded to be 3V. The charge-discharge profiles during the in situ measurements are in accordance with the redox signature from the cyclic voltammograms (CV) at scan rate of 0.1 mV/s. **Figure 4a, b** show the voltage profiles of 1st and 2nd charge-discharge cycles respectively, and **Figure 4c, d** show the corresponding in situ WAXS patterns at different voltages during the discharge and charge process. The WAXS pattern of the sample at OCV matches exactly the pattern of hexagonal MnO₂. During the lithiation and delithiation process, clear phase change of the oxide is observed, which is not reversible during the first cycle (**Figure 4c**). The phase obtained at the end of the first CD cycle is distinctively different from the original pattern of the pristine MnO₂. This newly formed phase undergoes a reversible transformation in the 2nd galvanostatic cycle (**Figure 4d**). The simulated position of the peaks of various materials along with appropriate references are summarized in **Table ST2** in the supporting information.

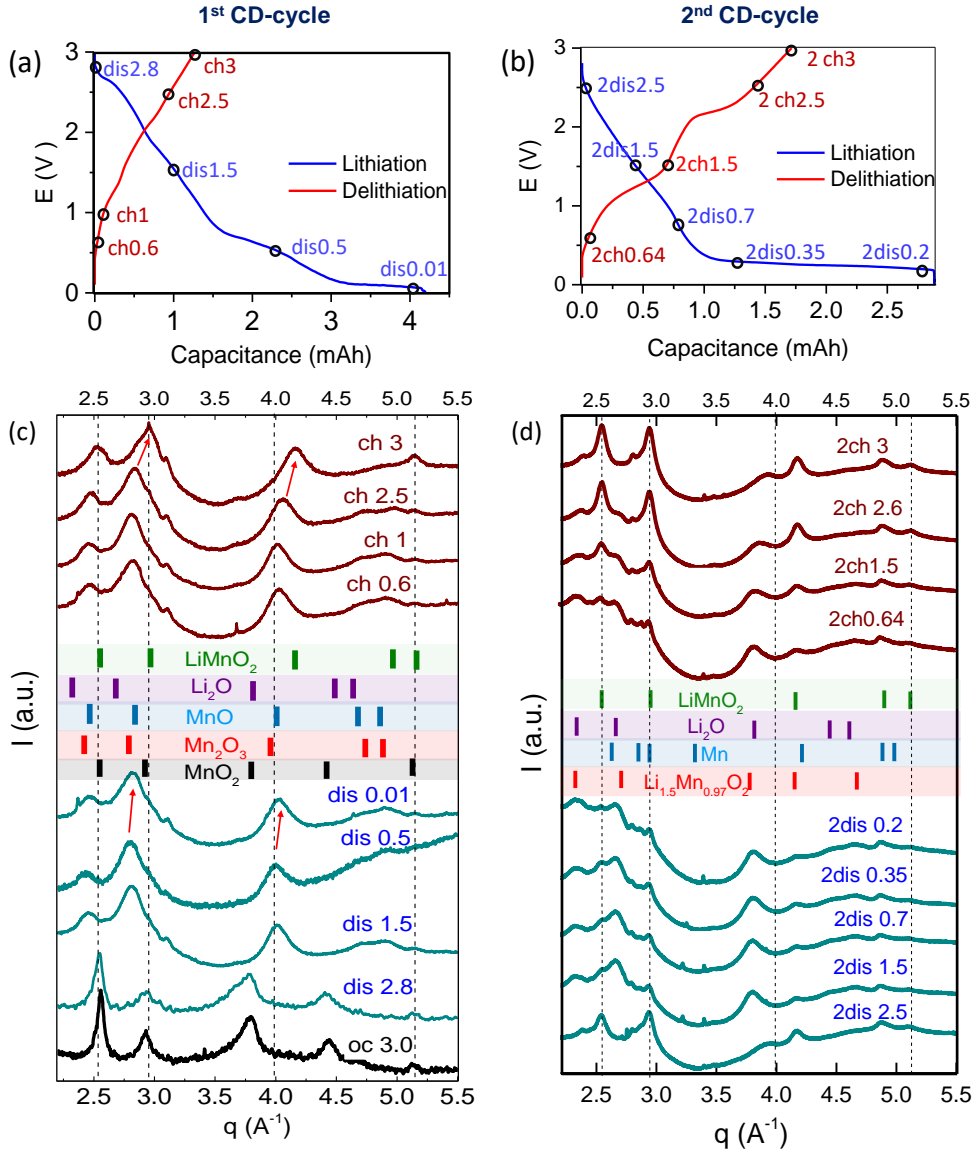
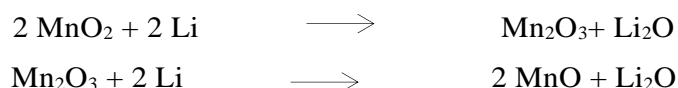


Figure 4. The voltage profiles (a, b) and corresponding in situ synchrotron X-ray scattering patterns (WAXS) (c, d) for the lithiation and delithiation process of 1st (a, c) and 2nd cycle (b, d) at a current density of 100 mA/g. In Figure c and d, the lithiation and delithiation process of 1st (a, c) and 2nd cycle (b, d) at a current density of 100 mA/g. In Figure c and d, the vertical lines correspond to the simulated patterns of different materials from the crystal structure database (ICSD, ICDD-PDF2).

The voltage profile of the first galvanostatic lithiation presents features of a pseudocapacitive process rather than an exclusive conversion process (**Figure 4a**). Part of the large irreversible capacity loss in the first cycle can be related to the formation of amorphous SEI layer on the high-surface area electrode. In addition, during the 1st discharge, as the voltage reaches 1.5 V, the peaks of hexagonal MnO_2 disappear and evolve to the orthorhombic phase of Mn_2O_3 . When the voltage drops further to 0.01V (complete lithiation) with a plateau, small shifts in the WAXS peak positions towards higher ' q ' were observed (shown with arrow in **Figure 4c**), which can be assigned to the diffraction pattern of the cubic phase of MnO. Further broadening of the peak

at 2.94 \AA^{-1} can be related to evolution of Li_2O . Due to broad nature of the WAXS peaks of the manganese oxides, the peaks corresponding to Li_2O could be merged with the ones of manganese oxide peaks, thus increasing their broadening at the end of the lithiation process (2.44 and 2.94 \AA^{-1}).

The process occurring during the first lithiation would thus consist of:



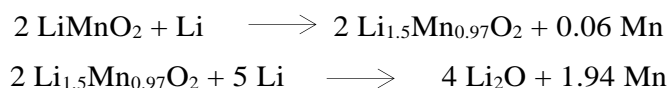
As shown in **Figure 4c**, with increasing voltage, the peaks corresponding to MnO slowly move toward higher q values. Considering the oxidation of the manganese center with gradual lithium extraction, the final WAXS pattern obtained at 3 V can be assigned to the orthorhombic LiMnO_2 . Therefore, the redox process during the 1st charging can be expressed as:



Unlike the charging profiles during the rate capability tests, in the first charging profile in the in situ WAXS measurement (delithiation process), there are hints of plateaus from the oxidation of metallic Mn to higher oxidation states. This implies that during the previous discharge process a small conversion of MnO_2 to metallic Mn and Li_2O cannot be neglected.

Interestingly, the voltage profile and the change in the in situ WAXS patterns during the 2nd galvanostatic cycle is distinctively different from the first one (**Figure 4b, d**). Here the discharge profile reaches a cathodic plateau at 0.4 V following a pseudocapacitive feature, whereas the charging profile has two distinct anodic signatures for a two-step oxidation process. During discharge, as the voltage reaches 1.5 V , the intensity of the peaks corresponding to LiMnO_2 decreases with the evolution of new sets of peaks that can be assigned to a more lithium rich manganese oxide with enhanced lattice spacing ($\text{Li}_{1.5}\text{Mn}_{0.97}\text{O}_2$), possibly through an intercalation process,⁶¹ which is consistent with the electron uptake by the active material. Upon further lithiation, this intermediate reduces to metallic Mn and Li_2O . During consecutive charging, slow evolution to LiMnO_2 was observed, which might involve the intermediate lithiated form of manganese oxide. A schematic diagram of the observed structural transformations of MnO_2 from in situ WAXS measurement is shown in **Figure 5**. The associated reactions are also included for reference below.

Second discharge



Second charge

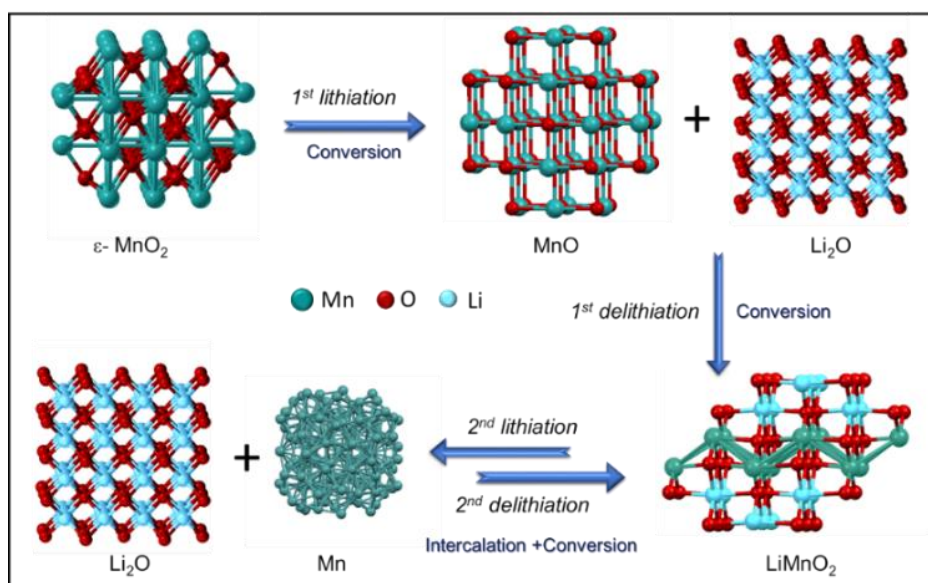
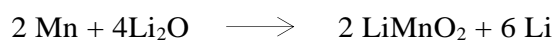


Figure 5. Schematic diagram for structural transformation of $\epsilon\text{-MnO}_2$ observed by in situ WAXS measurements.

These observations clarify the relation between Li storage mechanisms in MnO_2 anodes and the corresponding voltage profiles. Firstly, it can be inferred that even though MnO_2 was used as starting electroactive material, upon cycling in voltage window of 0-3V, the first conversion reaction is not reversible. Part of the irreversible capacity loss in the 1st cycle can be attributed to the irreversible lithium consumption by MnO_2 . Indeed, at the end of several galvanostatic cycles, the sample was found to contain significant amount of LiMnO_2 , rather than pristine MnO_2 structure (**Figure S8b**), which confirms that the newly formed LiMnO_2 has chemical reversibility upon electrochemical (EC) cycling. The same also can be inferred from the Raman spectrum of the EC cycled sample (**Figure S8c**). Apart from the signature D and G peaks from CNT, the strong peak at 600 cm^{-1} can be attributed to the stretching mode of Mn-O bonds, which has experienced significant red shift compared to that of the pristine material (**Figure 4d**). This can be delineated to decreased oxidation state of Mn and thereby decrease in the Mn-O bond energy. The smaller and broader peaks at $418, 467 \text{ cm}^{-1}$ and $245, 291 \text{ cm}^{-1}$ can be related to the deformation vibrations of the Mn-O-Mn bonds and vibrational modes of LiO_6 octahedra respectively.⁶⁵⁻⁶⁷ Furthermore, we confirmed the oxidation states of Mn in the samples after 1st complete lithiation and the following delithiation using X-ray photoelectron spectroscopy. **Figure S9** shows the high resolution XP spectra of Mn (3s) in the (a) pristine sample, (b) at 0 V (1st cycle) and (c) at 3V. Valence state of manganese ions was determined using the Galakhov

et al. approach⁶⁸, based on the splitting of the Mn 3s core-level spectrum from the exchange coupling between the Mn 3s hole and Mn 3d electrons. The magnitude of this splitting is proportional to $(2S + 1)$, where S is the local spin of the 3d electrons in the ground state. The differences in binding energy between these two peaks (ΔBE) were used to determine the average oxidation state of Mn at different states of lithiation, using values provided by Alvarez Galvan *et al* for reference.⁶⁹ Binding energy differences come out as 4.9, 5.8 and 5.3 eV, which correspond to (a) Mn^{4+} , (b) $Mn^{2.1+}$ and (c) $Mn^{3.1+}$ respectively. These results are in complete accordance with the findings from our in situ WAXS experiment. In this regard, it is noteworthy that when Li_2MnO_3 was used as anode material by Muhammad *et al.*, after 1st galvanostatic cyclic, it converted to cubic rock salt type $Li_{0.5}Mn_{0.5}O$ through the formation of Mn_3O_4 as intermediate.⁷⁰ In both the cases, +4 oxidation state of Mn reduces to +3 in the 1st CD cycle, which undergoes reversible conversion in the following cycles. Thus, the electrochemical reversibility of Mn^{4+} in such oxide rich environment is questionable.

These results also indicate that the nanostructured surface of this hybrid is beneficial to store significant amount of lithium through an intercalation process by increasing lithium concentration in the oxide. A similar increase in lithium concentration has been observed in MoO_3 anode,⁶¹ for example. But, to the best of our knowledge, the present work provides the first evidence of Li-ion storage by intercalation for manganese oxide-based Li-ion anodes. This also confirms that the charge storage mechanism for the region-(i) in the discharge profiles (*vide supra*) can be assigned to Li-ion storage by intercalation mechanism.

Finally, the in situ WAXS data during charge-discharge processes show a gradual reduction in relative intensity and broadening of the peaks, ascribed to progressive loss of crystallinity during the repeated conversion of the nanostructured inorganic phase.

Electrochemical stability

Equipped with the insights into the storage mechanism process, we evaluated the electrochemical stability of the hybrid material by galvanostatic cycling at different current densities. **Figure 6a, b and c** show the electrochemical stability of the $MnO_2@CNTF/Li$ upon galvanostatic cycling at current densities of 0.5, 1 and 5 A/g for 150, 300 and 1500 CD cycles respectively. When cycled at lower current densities (0.5 and 1 A/g), the $MnO_2/CNTF$ hybrid shows a slow increase in the capacity up to 200%. Similar phenomena also have been observed when Mn_3O_4 ,²⁹ MnO_2 ³² and Cu_2O-Li_2O ⁵⁵ were used as electroactive materials. During galvanostatic cycling at 0.5 A/g, the specific capacity gradually increases to 152% of its initial value. Similar enhancement in the capacitance is observed for galvanostatic cycling at 1 A/g current density; after 220 cycles an enhancement of 187% in specific capacitance is observed. After reaching the highest value, the capacity remains constant during rest of the cycling test. Throughout the CD cycling the coulombic efficiency remain around 100% (average 99.3%).

Very importantly, the specific capacity value at 5 A/g current density remains at 97 % of its original value, with near unity coulombic efficiency even after 1500 galvanostatic cycles. The electrochemical stability of this MnO₂@CNTF hybrid in half-cell configuration is comparable and even superior to some of the literature reports.^{18,42,43,71,72} This can be attributed to the presence of a stable interface between manganese oxide nanocrystals and carbon nanotubes, which not only buffers the structural change in the oxide layer, but also prevent agglomeration of the nanostructures during the charge–discharge process.

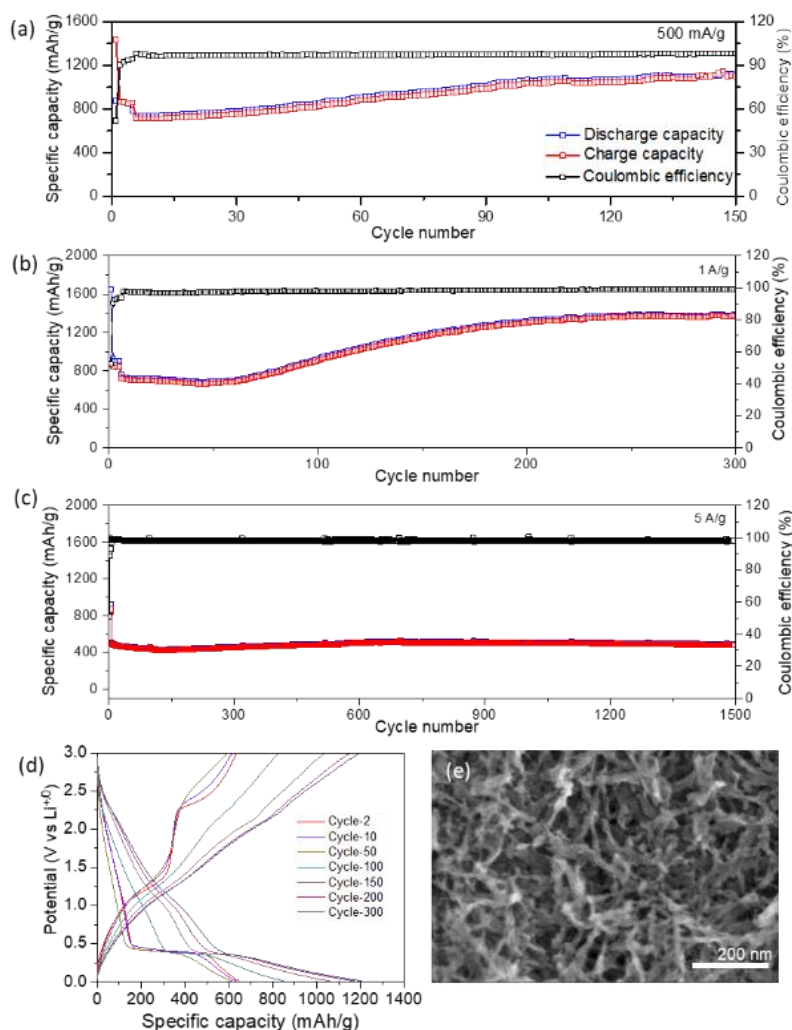


Figure 6. Stability of MnO₂@CNTF hybrid electrode over charge-discharge process of (a) 150 cycles at a current density of 0.5 A/g, (b) 300 cycles at a current density of 1 A/g and (c) 1500 cycles at a current density of 5 A/g. (d) The voltage profiles corresponding to graph (b) at cycle number 2, 10, 50, 100, 150, 200 and 300. (e) FESEM image of the post-cycled MnO₂@CNTF hybrid.

The origin of such increase in the specific capacity over CD cycling can be inferred from comparison of the voltage profiles, as shown in **Figure 6d** for 2, 10, 50, 100, 150, 200 and 300 cycles. Up to 50 cycles the voltage profiles are similar to those obtained in rate capability measurements, characterised by prominent redox plateaus for the conversion reactions. For

further cycles, the lithiation profile shows a decrease in the plateau corresponding to the reduction of manganese (region ii) at the expense of an increase in the pseudocapacitive regions (i) and (iii). Similarly, in the delithiation profiles the plateaus around 1.2 V and 2.4 V slowly disappear and the delithiation profiles during the late cycles resemble an almost straight charging profile. This indicates a clear increase in the pseudocapacitive processes compared to conversion reactions.

To understand this consecutive change in the mechanism of charge storage process, we performed ‘post-mortem’ analysis of the cycled electrode. Although direct observation of the active material is complicated by the presence of the SEI (**Figure S10**), there is evidence (**Figure 6d**) of the transformation of the original porous morphology of the MnO_2 elongated nanocrystals into a nanostructured coating around the CNT bundles, a process known as ‘electrochemical milling’.⁴⁴ During the conversion reactions the elongated interconnected MnO_2 nanocrystals gradually change shape without overall changes in crystal structure type, but with loss of crystallinity through the formation of new vacancies and grain boundaries. As amorphization of nanostructured LiMnO_2 progresses, Li storage by conversion is unfavourable and replaced by intercalation and pseudo capacitive processes. The defective structure can provide additional lithium storage sites, and together with possible increase in specific surface area, produce an increase of the pseudocapacitive contribution to total capacity. Indeed, a comparison of EIS spectra of the hybrid before and after electrochemical treatment shows a significant drop of $\sim 100\ \Omega$ in the charge-transfer resistance of the hybrid after cycling (see **Figure S12** and **Table ST3** in ESI).

Properties normalised by electrode weight

An important attribute of the hybrid material used in this work is that it already contains the current collector “built into it”. Combined with the high values of specific capacity discussed above, it makes MnO_2/CNTF hybrids attractive electrodes. As a reference for comparison, we produced conventional electrodes of commercial MnO_2 loaded with conducting carbon and 20 μm thick copper current collector (comm- $\text{MnO}_2\text{-C@Cu}$, $\sim 9\%$ MnO_2). The rate performance of the commercial comm- $\text{MnO}_2\text{-C@Cu}$ is shown in **Figure S13**, where the capacity values are normalized with respect to the total weight of the electrode. The specific capacity of the MnO_2/CNTF electrode is superior by at least an order of magnitude for all current densities. Taking the ratio of specific capacity of MnO_2/CNTF over the reference electrode, the improvement ranges from a factor of 18 at low current densities to a factor of 64 at high current density of 5 A/g (**Figure S13c**). Fully optimised electrodes would have a larger fraction of active material relative to current collector, however, this comparison helps illustrate benefits at device level of the architecture used here based on nanostructuring the active material by direct growth onto the porous, tough, CNTF current collector.

Conclusion

In conclusion, we have developed a flexible MnO_2 @CNT hybrids as anode materials for high performance Li-ion storage. The nanostructured morphology of the MnO_2 crystals is beneficial for the hybrid to achieve high Li capacity by providing additional surface storage sites. Using detailed electrochemical analysis, we determine that at low C-rate the charge storage mechanism mostly relies on the conversion mechanism, whereas at high C rate, the contribution of pseudocapacitive process is dominant. The high surface area of this hybrid helps to achieve a specific capacity value in excess of 1100 and 500 mAh/g at a discharge current density of 25 mA/g and 5 A/g, respectively. From the in situ WAXS measurements, an irreversible phase change of ϵ - MnO_2 to LiMnO_2 was observed in the first cycle. Therefore, part of the irreversible capacity loss in the 1st galvanostatic cycle is related to the irreversible lithium consumption by the redox active phase. In subsequent galvanostatic cycles the phase changes are reversible. We found that, at a moderate discharge rate, the storage of lithium occurs possibly through an intercalation process, followed by a conversion mechanism.

The MnO_2 @CNT hybrid has shown interesting stability profile on galvanostatic cycling, where the specific capacity gradually increases up to 200%. Our post-mortem investigations reveal that upon cycling, the interconnected porous nanocrystals of MnO_2 undergo ‘electrochemical milling’, that results in generation of new surface storage sites, drastic change in the morphology of the oxide around CNTF along with an increase in the interface area between the oxide and CNTF. All of these effects enhanced specific capacity. Finally, we found that at high current density, the free-standing MnO_2 @CNTF hybrid can provide up to 64 times higher specific capacity compared to a reference electrodes produced with commercial MnO_2 on a metallic current collector.

Our results establish that use of freestanding ϵ - MnO_2 @CNTF anode is highly promising for light weight, flexible, lithium ion storage devices. The architecture of nanocrystals of MnO_2 directly anchored on CNTF provides low electrical resistance and stability to contain volumetric expansions during intercalation and conversion processes. But ultimately, the electrochemically reversible phase for lithium storage is found to be LiMnO_2 , rather than parent MnO_2 . Work is in progress to investigate hybrids with other transition metal oxides and revisit the premise of reversible conversion of the initial material.

Acknowledgements

M.R. and J.J.V. are grateful for generous financial support provided by the European Union Seventh Framework Program under grant agreement 678565 (ERC-STEM) and 648319 (ERC-HyMAP) the Clean Sky Joint Undertaking 2, Horizon 2020 under Grant Agreement Number 738085 (SORCERER), by MINECO (RyC-2014-15115) and FotoArt-CM (S2018/NMT-4367).

N. B. acknowledges Comunidad de Madrid for the post-doctoral fellowship 2018-T2/AMB-12025. The authors thank NCD-SWEET beamline staff at ALBA Synchrotron Light Facility for assistance with synchrotron experiments.

References

- (1) Park, S.-H.; King, P. J.; Tian, R.; Boland, C. S.; Coelho, J.; Zhang, C. (John); McBean, P.; McEvoy, N.; Kremer, M. P.; Daly, D.; et al. High Areal Capacity Battery Electrodes Enabled by Segregated Nanotube Networks. *Nat. Energy* **2019**.
- (2) Li, M.; Lu, J.; Chen, Z.; Amine, K. 30 Years of Lithium-Ion Batteries. *Adv. Mater.* **2018**, *30* (33), 1800561.
- (3) Schäfer, A. W.; Barrett, S. R. H.; Doyme, K.; Dray, L. M.; Gnad, A. R.; Self, R.; O'Sullivan, A.; Synodinos, A. P.; Torija, A. J. Technological, Economic and Environmental Prospects of All-Electric Aircraft. *Nat. Energy* **2019**, *4* (2), 160–166.
- (4) Wagner, F. T.; Lakshmanan, B.; Mathias, M. F. Electrochemistry and the Future of the Automobile. *J. Phys. Chem. Lett.* **2010**, *1* (14), 2204–2219.
- (5) Xu, Q.; Li, J.-Y.; Sun, J.-K.; Yin, Y.-X.; Wan, L.-J.; Guo, Y.-G. Watermelon-Inspired Si/C Microspheres with Hierarchical Buffer Structures for Densely Compacted Lithium-Ion Battery Anodes. *Adv. Energy Mater.* **2017**, *7* (3), 1601481.
- (6) Li, S.; Niu, J.; Zhao, Y. C.; So, K. P.; Wang, C.; Wang, C. A.; Li, J. High-Rate Aluminium Yolk-Shell Nanoparticle Anode for Li-Ion Battery with Long Cycle Life and Ultrahigh Capacity. *Nat. Commun.* **2015**, *6*, 7872.
- (7) Zhao, Y.; Wang, L. P.; Sougrati, M. T.; Feng, Z.; Leconte, Y.; Fisher, A.; Srinivasan, M.; Xu, Z. A Review on Design Strategies for Carbon Based Metal Oxides and Sulfides Nanocomposites for High Performance Li and Na Ion Battery Anodes. *Adv. Energy Mater.* **2017**, *7* (9), 1601424.

- (8) Qian, G.; Liao, X.; Zhu, Y.; Pan, F.; Chen, X.; Yang, Y. Designing Flexible Lithium-Ion Batteries by Structural Engineering. *ACS Energy Lett.* **2019**, *4* (3), 690–701.
- (9) Mo, R.; Rooney, D.; Sun, K.; Yang, H. Y. 3D Nitrogen-Doped Graphene Foam with Encapsulated Germanium/Nitrogen-Doped Graphene Yolk-Shell Nanoarchitecture for High-Performance Flexible Li-Ion Battery. *Nat. Commun.* **2017**, *8*, 13949.
- (10) Elango, R.; Demortière, A.; De Andrade, V.; Morcrette, M.; Seznec, V. Thick Binder-Free Electrodes for Li-Ion Battery Fabricated Using Templating Approach and Spark Plasma Sintering Reveals High Areal Capacity. *Adv. Energy Mater.* **2018**, *8* (15), 1703031.
- (11) Blomgren, G. E. The Development and Future of Lithium Ion Batteries. *J. Electrochem. Soc.* **2017**, *164* (1), A5019–A5025.
- (12) Tao, T.; Lu, S.; Chen, Y. A Review of Advanced Flexible Lithium-Ion Batteries. *Adv. Mater. Technol.* **2018**, *3* (9), 1700375.
- (13) AbdelHamid, A. A.; Yu, Y.; Yang, J.; Ying, J. Y. Generalized Synthesis of Metal Oxide Nanosheets and Their Application as Li-Ion Battery Anodes. *Adv. Mater.* **2017**, *29* (32), 1701427.
- (14) Zheng, M.; Tang, H.; Li, L.; Hu, Q.; Zhang, L.; Xue, H.; Pang, H. Hierarchically Nanostructured Transition Metal Oxides for Lithium-Ion Batteries. *Adv. Sci.* **2018**, *5* (3), 1700592.
- (15) Huang, S.-Z.; Cai, Y.; Jin, J.; Liu, J.; Li, Y.; Wang, H.-E.; Chen, L.-H.; Hasan, T.; Su, B.-L. Unique Walnut-Shaped Porous MnO₂/C Nanospheres with Enhanced Reaction Kinetics for Lithium Storage with High Capacity and Superior Rate Capability. *J. Mater. Chem. A* **2016**, *4* (11), 4264–4272.
- (16) Henzie, J.; Etacheri, V.; Jahan, M.; Rong, H.; Hong, C. N.; Pol, V. G. Biomineralization-Inspired Crystallization of Monodisperse α -Mn₂O₃ Octahedra and Assembly of High-Capacity Lithium-Ion Battery Anodes. *J. Mater. Chem. A* **2017**, *5* (13), 6079–6089.

- (17) Wang, X.; Ma, L.; Ji, Q.; Meng, J.-Q.; Liang, S.; Xu, Z.; Wang, M.; Zuo, X.; Xiao, Y.; Zhu, J.; et al. MnO/Metal/Carbon Nanohybrid Lithium-Ion Battery Anode With Enhanced Electrochemical Performance: Universal Facile Scalable Synthesis and Fundamental Understanding. *Adv. Mater. Interfaces* **2019**, *6* (12), 1900335.
- (18) Voskanyan, A. A.; Ho, C.-K.; Chan, K. Y. 3D δ -MnO₂ Nanostructure with Ultralarge Mesopores as High-Performance Lithium-Ion Battery Anode Fabricated via Colloidal Solution Combustion Synthesis. *J. Power Sources* **2019**, *421*, 162–168.
- (19) Shin, J.-Y.; Samuelis, D.; Maier, J. Sustained Lithium-Storage Performance of Hierarchical, Nanoporous Anatase TiO₂ at High Rates: Emphasis on Interfacial Storage Phenomena. *Adv. Funct. Mater.* **2011**, *21* (18), 3464–3472.
- (20) Tarascon, J.-M.; Armand, M. Issues and Challenges Facing Rechargeable Lithium Batteries. In *Materials for Sustainable Energy*; Co-Published with Macmillan Publishers Ltd, UK, 2010; pp 171–179.
- (21) Poizot, P.; Laruelle, S.; Grugeon, S.; Dupont, L.; Tarascon, J.-M. Nano-Sized Transition-Metal Oxides as Negative-Electrode Materials for Lithium-Ion Batteries. *Nature* **2000**, *407* (6803), 496–499.
- (22) Lu, Y.; Yu, L.; Lou, X. W. (David). Nanostructured Conversion-Type Anode Materials for Advanced Lithium-Ion Batteries. *Chem* **2018**, *4* (5), 972–996.
- (23) Etacheri, V.; Marom, R.; Elazari, R.; Salitra, G.; Aurbach, D. Challenges in the Development of Advanced Li-Ion Batteries: A Review. *Energy Environ. Sci.* **2011**, *4* (9), 3243–3262.
- (24) Chen, Y.; Fu, K.; Zhu, S.; Luo, W.; Wang, Y.; Li, Y.; Hitz, E.; Yao, Y.; Dai, J.; Wan, J.; et al. Reduced Graphene Oxide Films with Ultrahigh Conductivity as Li-Ion Battery Current Collectors. *Nano Lett.* **2016**, *16* (6), 3616–3623.
- (25) Jiang, H.; Hu, Y.; Guo, S.; Yan, C.; Lee, P. S.; Li, C. Rational Design of MnO/Carbon Nanopeapods with Internal Void Space for High-Rate and Long-Life Li-Ion Batteries. *ACS*

Nano **2014**, 8 (6), 6038–6046.

- (26) Moumita Rana, Cleis Santos, Alfonso Monreal-Bernal, J. J. V. CNT Fibre-Based Hybrids: Synthesis, Characterization and Applications in Energy Management. In *Nanocarbons and their hybrids: from synthesis to applications*; Wiley, 2019; p Submitted.
- (27) Bruce, P. G.; Scrosati, B.; Tarascon, J.-M. Nanomaterials for Rechargeable Lithium Batteries. *Angew. Chemie Int. Ed.* **2008**, 47 (16), 2930–2946.
- (28) Bai, M.; Xie, K.; Yuan, K.; Zhang, K.; Li, N.; Shen, C.; Lai, Y.; Vajtai, R.; Ajayan, P.; Wei, B. A Scalable Approach to Dendrite-Free Lithium Anodes via Spontaneous Reduction of Spray-Coated Graphene Oxide Layers. *Adv. Mater.* **2018**, 30 (29), 1801213.
- (29) Wang, J.-G.; Liu, H.; Zhou, R.; Liu, X.; Wei, B. Onion-like Nanospheres Organized by Carbon Encapsulated Few-Layer MoS₂ Nanosheets with Enhanced Lithium Storage Performance. *J. Power Sources* **2019**, 413, 327–333.
- (30) Tan, X.; Guo, L.; Liu, S.; Wu, J.; Zhao, T.; Ren, J.; Liu, Y.; Kang, X.; Wang, H.; Sun, L.; et al. A General One-Pot Synthesis Strategy of 3D Porous Hierarchical Networks Crosslinked by Monolayered Nanoparticles Interconnected Nanoplates for Lithium Ion Batteries. *Adv. Funct. Mater.* **2019**, 0 (0), 1903003.
- (31) Tang, L.; Zhang, R.; Zhang, X.; Zhao, N.; Shi, C.; Liu, E.; Ma, L.; Luo, J.; He, C. ZnO Nanoconfined 3D Porous Carbon Composite Microspheres to Stabilize Lithium Nucleation/Growth for High-Performance Lithium Metal Anodes. *J. Mater. Chem. A* **2019**.
- (32) He, X.; Tian, L.; Qiao, M.; Zhang, J.; Geng, W.; Zhang, Q. A Novel Highly Crystalline Fe₄(Fe(CN)₆)₃ Concave Cube Anode Material for Li-Ion Batteries with High Capacity and Long Life. *J. Mater. Chem. A* **2019**, 7 (18), 11478–11486.
- (33) Chen, B.; Wang, Y.; Chang, Z.; Li, M.; Liu, X.; Zhang, L.; Wang, X. Enhanced Capacitive Desalination of MnO₂ by Forming Composite with Multi-Walled Carbon Nanotubes. *RSC Adv.* **2016**, 6 (8), 6730–6736.

- (34) Wu, Y.; Li, X.; Xiao, Q.; Lei, G.; Li, Z.; Guan, J. The Coaxial MnO₂/CNTs Nanocomposite Freestanding Membrane on SSM Substrate as Anode Materials in High Performance Lithium Ion Batteries. *J. Electroanal. Chem.* **2019**, *834*, 161–166.
- (35) Grundish, N. S.; Amos, C. D.; Agrawal, A.; Khani, H.; Goodenough, J. B. Low-Cost Self-Assembled Oxide Separator for Rechargeable Batteries. *Adv. Funct. Mater.* **2019**, *0* (0), 1903550.
- (36) Augustyn, V.; Simon, P.; Dunn, B. Pseudocapacitive Oxide Materials for High-Rate Electrochemical Energy Storage. *Energy Environ. Sci.* **2014**, *7* (5), 1597–1614.
- (37) Deng, X.; Wei, Z.; Cui, C.; Liu, Q.; Wang, C.; Ma, J. Oxygen-Deficient Anatase TiO₂@C Nanospindles with Pseudocapacitive Contribution for Enhancing Lithium Storage. *J. Mater. Chem. A* **2018**, *6* (9), 4013–4022.
- (38) Goriparti, S.; Miele, E.; De Angelis, F.; Di Fabrizio, E.; Proietti Zaccaria, R.; Capiglia, C. Review on Recent Progress of Nanostructured Anode Materials for Li-Ion Batteries. *J. Power Sources* **2014**, *257*, 421–443.
- (39) Chen, J.; Wang, Y.; He, X.; Xu, S.; Fang, M.; Zhao, X.; Shang, Y. Electrochemical Properties of MnO₂ Nanorods as Anode Materials for Lithium Ion Batteries. *Electrochim. Acta* **2014**, *142*, 152–156.
- (40) Li, H.; Zhang, X.; Zhu, Y.; Li, R.; Chen, H.; Gao, P.; Zhang, Y.; Li, T.; Liu, Y.; Li, Q. Hydrothermal Deposition of a Zinc Oxide Nanorod Array on a Carbon Nanotube Film as a Piezoelectric Generator. *RSC Adv.* **2014**, *4* (82), 43772–43777.
- (41) Pendashteh, A.; Senokos, E.; Palma, J.; Anderson, M.; Vilatela, J. J.; Marcilla, R. Manganese Dioxide Decoration on Macroscopic CNT Fibers: From High-Performance Liquid-Based to All-Solid-State Supercapacitors. *J. Power Sources* **2017**, *372*, 64–73.
- (42) Zang, J.; Ye, J.; Qian, H.; Lin, Y.; Zhang, X.; Zheng, M.; Dong, Q. Hollow Carbon Sphere with Open Pore Encapsulated MnO₂ Nanosheets as High-Performance Anode Materials for

Lithium Ion Batteries. *Electrochim. Acta* **2018**, *260*, 783–788.

- (43) Shen, L.; Dong, Q.; Zhu, G.; Dai, Z.; Zhang, Y.; Wang, W.; Dong, X. Versatile MnO₂/CNT Putty-Like Composites for High-Rate Lithium-Ion Batteries. *Adv. Mater. Interfaces* **2018**, *5* (14), 1800362.
- (44) Chen, C.; Ding, N.; Wang, L.; Yu, Y.; Lieberwirth, I. Some New Facts on Electrochemical Reaction Mechanism for Transition Metal Oxide Electrodes. *J. Power Sources* **2009**, *189* (1), 552–556.
- (45) Fang, X.; Lu, X.; Guo, X.; Mao, Y.; Hu, Y.-S.; Wang, J.; Wang, Z.; Wu, F.; Liu, H.; Chen, L. Electrode Reactions of Manganese Oxides for Secondary Lithium Batteries. *Electrochem. commun.* **2010**, *12* (11), 1520–1523.
- (46) Ren, Y.; Armstrong, A. R.; Jiao, F.; Bruce, P. G. Influence of Size on the Rate of Mesoporous Electrodes for Lithium Batteries. *J. Am. Chem. Soc.* **2010**, *132* (3), 996–1004.
- (47) Kundu, M.; Ng, C. C. A.; Petrovykh, D. Y.; Liu, L. Nickel Foam Supported Mesoporous MnO₂ Nanosheet Arrays with Superior Lithium Storage Performance. *Chem. Commun.* **2013**, *49* (76), 8459–8461.
- (48) Reguero, V.; Alemán, B.; Mas, B.; Vilatela, J. J. Controlling Carbon Nanotube Type in Macroscopic Fibers Synthesized by the Direct Spinning Process. *Chem. Mater.* **2014**, *26* (11), 3550–3557.
- (49) Senokos, E.; Reguero, V.; Palma, J.; Vilatela, J. J.; Marcilla, R. Macroscopic Fibres of CNTs as Electrodes for Multifunctional Electric Double Layer Capacitors: From Quantum Capacitance to Device Performance. *Nanoscale* **2016**, *8* (6), 3620.
- (50) Senokos, E.; Rana, M.; Santos, C.; Marcilla, R.; Vilatela, J. J. Controlled Electrochemical Functionalization of CNT Fibers: Structure-Chemistry Relations and Application in Current Collector-Free All-Solid Supercapacitors. *Carbon N. Y.* **2019**, *142*, 599–609.
- (51) Boaretto, Nicola; Almenara, Jesús; Mikhalchan, Anastasiia; Marcilla, Rebeca; VILATELA, J.

- J. A Route to High-Toughness Battery Electrodes. *ACS Appl. Energy Mater.* **2019**, under revision.
- (52) Kondrashev, Y. D.; Zaslavskii, A. I. The Structure of the Modifications of Manganese (IV) Oxide. *Izv. Akad. Nauk SSSR, Seriya Fiz.* **1951**, *15*, 179–186.
- (53) Pendashteh, A.; Senokos, E.; Palma, J.; Anderson, M.; Vilatela, J. J.; Marcilla, R. Manganese Dioxide Decoration of Macroscopic Carbon Nanotube Fibers: From High-Performance Liquid-Based to All-Solid-State Supercapacitors. *J. Power Sources* **2017**, *372*, 64–73.
- (54) He, G.; Duan, Y.; Song, L.; Zhang, X. Doping Strategy to Boost Electromagnetic Property and Gigahertz Tunable Electromagnetic Attenuation of Hetero-Structured Manganese Dioxide. *Dalt. Trans.* **2019**, *48* (7), 2407–2421.
- (55) Xie, Y.; Yu, Y.; Gong, X.; Guo, Y.; Guo, Y.; Wang, Y.; Lu, G. Effect of the Crystal Plane Figure on the Catalytic Performance of MnO₂ for the Total Oxidation of Propane. *CrystEngComm* **2015**, *17* (15), 3005–3014.
- (56) Julien, C.; Massot, M.; Rangan, S.; Lemal, M.; Guyomard, D. Study of Structural Defects in Γ -MnO₂ by Raman Spectroscopy. *J. Raman Spectrosc.* **2002**, *33* (4), 223–228.
- (57) Aksel, S.; Eder, D. Catalytic Effect of Metal Oxides on the Oxidation Resistance in Carbon Nanotube – Inorganic Hybrids †. **2010**.
- (58) Shannon, R. D. Revised Effective Ionic Radii and Systematic Studies of Interatomic Distances in Halides and Chalcogenides. *Acta Crystallogr. Sect. A Cryst. physics, diffraction, Theor. Gen. Crystallogr.* **1976**, *32* (5), 751–767.
- (59) Liu, Q.; Cresce, A.; Schroeder, M.; Xu, K.; Mu, D.; Wu, B.; Shi, L.; Wu, F. Insight on Lithium Metal Anode Interphasial Chemistry: Reduction Mechanism of Cyclic Ether Solvent and SEI Film Formation. *Energy Storage Mater.* **2019**, *17*, 366–373.
- (60) Yue, J.; Gu, X.; Jiang, X.; Chen, L.; Wang, N.; Yang, J.; Ma, X. Coaxial Manganese Dioxide@ N-Doped Carbon Nanotubes as Superior Anodes for Lithium Ion Batteries.

Electrochim. Acta **2015**, *182*, 676–681.

- (61) Shon, J. K.; Lee, H. S.; Park, G. O.; Yoon, J.; Park, E.; Park, G. S.; Kong, S. S.; Jin, M.; Choi, J.-M.; Chang, H. Discovery of Abnormal Lithium-Storage Sites in Molybdenum Dioxide Electrodes. *Nat. Commun.* **2016**, *7*, 11049.
- (62) Liu, T.; Pell, W. G.; Conway, B. E.; Roberson, S. L. Behavior of Molybdenum Nitrides as Materials for Electrochemical Capacitors Comparison with Ruthenium Oxide. *J. Electrochem. Soc.* **1998**, *145* (6), 1882–1888.
- (63) Wang, J.; Polleux, J.; Lim, J.; Dunn, B. Pseudocapacitive Contributions to Electrochemical Energy Storage in TiO₂ (Anatase) Nanoparticles. *J. Phys. Chem. C* **2007**, *111* (40), 14925–14931.
- (64) Cao, K.; Jin, T.; Yang, L.; Jiao, L. Recent Progress in Conversion Reaction Metal Oxide Anodes for Li-Ion Batteries. *Mater. Chem. Front.* **2017**, *1* (11), 2213–2242.
- (65) Zhao, L. Z.; Chen, Y. W.; Wang, G. R. Raman Spectra Study of Orthorhombic LiMnO₂. *Solid State Ionics* **2010**, *181* (31), 1399–1402.
- (66) Hwang, S.-J.; Park, H.-S.; Choy, J.-H.; Campet, G.; Portier, J.; Kwon, C.-W.; Etourneau, J. Micro-Raman Spectroscopic Study on Layered Lithium Manganese Oxide and Its Delithiated/Relithiated Derivatives. *Electrochem. Solid-State Lett.* **2001**, *4* (12), A213–A216.
- (67) Ruther, R. E.; Callender, A. F.; Zhou, H.; Martha, S. K.; Nanda, J. Raman Microscopy of Lithium-Manganese-Rich Transition Metal Oxide Cathodes. *J. Electrochem. Soc.* **2015**, *162* (1), A98–A102.
- (68) Galakhov, V. R.; Demeter, M.; Bartkowski, S.; Neumann, M.; Ovechkina, N. A.; Kurmaev, E. Z.; Lobachevskaya, N. I.; Mukovskii, Y. M.; Mitchell, J.; Ederer, D. L. Mn 3 s Exchange Splitting in Mixed-Valence Manganites. *Phys. Rev. B* **2002**, *65* (11), 113102.
- (69) Álvarez-Galván, M. C.; de La Peña O'Shea, V. A.; Arzamendi, G.; Pawelec, B.; Gandía, L. M.; Fierro, J. L. G. Methyl Ethyl Ketone Combustion over La-Transition Metal (Cr, Co, Ni,

- Mn) Perovskites. *Appl. Catal. B Environ.* **2009**, 92 (3–4), 445–453.
- (70) Muhammad, S.; Yun, S.; Palanisamy, K.; Kim, H.; Yoon, W.-S. Mechanistic Studies on Reversible Conversion Reaction in Li_2MnO_3 -Carbon Nanotube Composite Anode. *J. Power Sources* **2019**, 423, 323–330.
- (71) Liu, K.; Zou, F.; Sun, Y.; Yu, Z.; Liu, X.; Zhou, L.; Xia, Y.; Vogt, B. D.; Zhu, Y. Self-Assembled $\text{Mn}_3\text{O}_4/\text{C}$ Nanospheres as High-Performance Anode Materials for Lithium Ion Batteries. *J. Power Sources* **2018**, 395, 92–97.
- (72) Zhang, D.; Li, G.; Fan, J.; Li, B.; Li, L. In Situ Synthesis of Mn_3O_4 Nanoparticles on Hollow Carbon Nanofiber as High-Performance Lithium-Ion Battery Anode. *Chem. – A Eur. J.* **2018**, 24 (38), 9632–9638.